Supporting Information

Title

Self-sensing robotic structures from architectured particle assemblies

*Xudong Yang, Zongzheng Wang, Bojian Zhang, Tianyu Chen, Changhong Linghu, Kunlin Wu, Guohui Wang, Hailu Wang, Yifan Wang**

This PDF file includes:

Supplementary Text
Figs. S1 to S12
Tables S1 to S2

Other Supplementary Materials for this manuscript include the following:
Movies S1 to S3

Supplementary Text

Elastic contact resistance of 3D printed surface with coating

The contact between the rough surfaces with coating is a realistic and universal phenomenon and has always been the subject of attention. The surface manufactured by 3D printing is naturally rough with characteristics of multi-scale and uncertainty, which makes it difficult to solve contact problems. Currently there are three methods, namely statistical approach [1], finite element methods (FEM) [2] and numerical solution [3] to solve the problem. Considering the first method being unable to capture the real characteristics of the rough surface and the time-consuming characteristic of the second method, here we adopt the third method to model the contact between conductive architectured particles.

When two rough surfaces are in contact with each other under an external applied load, the contact pressure will be generated on the asperities, resulting in a discrete pressure distribution. The two surfaces will deform elastically inward under this discrete pressure distribution. The gap distribution between the two deformed contact surfaces is defined as

$$h(x,y) = h_0 + f(x,y) + v_1(x,y) + v_2(x,y) + \delta_1(x,y) + \delta_2(x,y) \qquad (1)$$

where h_0 is rigid-body approach. $f(x, y)$ is original macro geometry of the contact bodies. v_1 and v_2 represent the elastic deformation of two coated surfaces. δ_1 and δ_2 indicate the roughness of two coated surfaces.

The contact elastic deformation of coated surface is obtained by using a discrete convolution and fast Fourier transform (DC-FFT) method [4]. According to Boussinesq integral equation, the calculation formula of individual surface elastic deformation under a certain pressure distribution can generally be given as

$$v(x,y) = \frac{1}{\pi E'} \iint_{\Omega} R(\xi - x, \varsigma - y)\, p(\xi,\varsigma)\, d\xi\, d\varsigma \qquad (2)$$

where E' indicates reduced young's modulus. The above equation is a typical convolution form. Applying the Fourier transform on both sides of Eq. (2), the following equation can be derived as

$$V(m,n) = \overline{R}(m,n) P(m,n) \qquad (3)$$

where $V(m,n)$ and $P(m,n)$ is the Fourier transform of $v(x, y)$ and $p(\xi,\varsigma)$, respectively. $\overline{R}(m,n)$ is the transfer function in frequency domain. For a coated surface, $\overline{R}(m,n)$ are given by Ref. [5] and is expressed as

$$\overline{R}(m,n) = \frac{2(1 + 4\omega l \kappa\varepsilon - \lambda\kappa\varepsilon^2)}{E_c' \omega [1 - (\lambda + \kappa + 4\kappa\omega^2 l^2)\varepsilon + \lambda\kappa\varepsilon^2]} \qquad (4)$$

where

$$\begin{aligned}
\kappa &= \frac{\mu-1}{\mu+(3-4\nu_c)} \\
\lambda &= 1-\frac{4(1-\nu_c)}{1+\mu(3-4\nu_s)} \\
\omega &= \sqrt{m^2+n^2} \\
E_c' &= \frac{E_c}{1-\nu_c^2} \\
\mu &= \frac{E_c(1+\nu_s)}{E_s(1+\nu_c)} \\
\varepsilon &= \exp(-2\omega l)
\end{aligned} \qquad (5)$$

where l is coating thickness. E_c and E_s is the young's modulus of coating and substrate, ν_c and ν_s is the Poisson's ratio of coating and substrate, respectively. E_c' represents the equivalent young's modulus of coating.

The transfer function in frequency domain (Eq. 4) is discretized at denser grid points than the computing grid to weaken the aliasing effect. In addition, the singularity at w=0 is removed by Gauss quadrature. After that, the distribution of surface elastic deformation in frequency domain is calculated by Eq. (3). Finally, the inverse Fourier transform is used to transform the surface elastic deformation from the frequency domain to space domain.

The contact solution of coated rough surface includes the solution of the contact pressure and gap distribution, as well as the determination of the contact area in entire solution domain. Assuming no tensile stress and surface penetration, this results in non-negative constraints of contact pressure and gap. Combining Eqs. (1-5), a linear complementary system can be mathematically constructed for coated rough surface contact problem and expressed as

$$\begin{cases}
-v_1(x,y)-v_2(x,y) = h_0 + f(x,y)+\delta_1(x,y)+\delta_2(x,y) & \text{where } p(x,y)>0 \\
-v_1(x,y)-v_2(x,y) < h_0 + f(x,y)+\delta_1(x,y)+\delta_2(x,y) & \text{where } p(x,y)=0 \\
F = \iint_\Omega p(x,y)dxdy
\end{cases} \qquad (6)$$

where F is applied load, Ω is computational domain.

The conjugate gradient technique [3a] is adopted to solve the linear complementary system above. The detailed solution process, readers can refer to the Ref. [3a].

With the model above, the real contact area A_c of two coated particles can be obtained. Then contact resistance between the two coated rough surfaces can be calculated based on the tunnelling current [6]:

$$R_c = \frac{c^2 s}{A_c e^2\sqrt{2m\varphi}}\exp\left(\frac{4\pi s\sqrt{2m\varphi}}{c}\right) \qquad (7)$$

where c indicates the Planck's constant. s stand for tunnelling distance. m is electronic quality. φ is potential barrier height. e is electron charge.

Results and discussion

To investigate the real contact of 3D printing surface with coating, the 3D surface topography of the particle is measured by laser confocal microscope (Figure S7). As shown, the roughness of particle is distributed in strips, and the maximum roughness asperity is about 18 μm. Two 3D roughness profiles will be superimposed on the two contact surfaces respectively to perform the contact analysis. Setting $f(x, y)=0$, which indicates two nominally flat rough surfaces contact. The solution domain is 500 x 500 μm. The coating thickness is 22 nm as measured in Ref. [7]. The Young's modulus of the gold coating is E_c=70 GPa and and the Poisson's ratio is ν_c=0.42 [8]. The Young's modulus and Poisson's ratio of the 3D printed particles are E_s=2.2 GPa and ν_s=0.3, respectively. In addition, a maximum pressure of 65 MPa is set in numerical solution to represent the plastic yielding of the material.

Based on the method, the obtained pressure and gap distributions with an applied pressure of 1MPa are shown in Figure S9. As shown, the gap distribution between the rough contact surfaces ranges from 0 μm to 30 μm. The contact occurs where the superimposed roughness of the two surfaces is greatest, which corresponds to the region where the gap is zero. Pressure will be generated at the point of contact, and it is easy to cause stress concentration due to the large roughness of the 3D printed surface.

According to the tunnelling current (Eq. 7), the resistance of contact is inversely proportional to the contact area. Here a comparison of experimental measurement and numerical simulation of contact resistance change rate of real 3D printed surface with coating was performed as shown in Figure 3c. As shown, both experimental and simulation results reveal that the resistance reduction rate increases with the increase of the pressure, and the two results are in good agreement.

Here the contact between two trapezoidal particles under three-point bending is also investigated. In fact, the contact between adjacent particles will convert from surface contact to line contact under three-point bending load. Changing $f(x, y)$ to the corresponding line contact geometry, the linear elastic contact of real 3D printed surface with coating can be solved using the method above. Noted that the applied load is obtained from the three-point bending finite element analysis. 500 um of the line contact is used for numerical simulation, the contact pressure and gap distribution of one of the cases are shown in Figure S9 & S10. As shown in Figure 3d, there is good agreement between the average contact stress and the contact area, the greater the contact force, the greater the contact area, which leads to a lower resistance.

References

[1] a) J. A. Greenwood, J. P. Williamson, *Proceedings of the royal society of London. Series A. Mathematical and physical sciences* **1966**, 295, 300; b) R. L. Jackson, I. Green, *Tribology International* **2006**, 39, 906.

[2] a) G. Liu, J. Zhu, L. Yu, Q. J. Wang, *Tribology transactions* **2001**, 44, 437; b) L. Pei, S. Hyun, J. Molinari, M. O. Robbins, *Journal of the Mechanics and Physics of Solids* **2005**, 53, 2385.

[3] a) I. Polonsky, L. Keer, *Wear* **1999**, 231, 206; b) Y.-Z. Hu, G. C. Barber, D. Zhu, *Tribology transactions* **1999**, 42, 443.

[4] a) S. Liu, Q. Wang, G. Liu, *Wear* **2000**, 243, 101; b) Y. Liu, W. Wayne Chen, D. Zhu, S. Liu, Q. J. Wang, **2007**.

[5] T. O'sullivan, R. King, **1988**.

[6] a) J. G. Simmons, *Journal of Applied Physics* **1963**, 34, 1793; b) H. Yang, J.-C. Shang, W.-F. Wang, Y.-F. Yang, Y.-N. Yuan, H.-S. Lei, D.-N. Fang, *Composites Science and Technology* **2022**, 221.

[7] L. Romano-Brandt, E. Salvati, E. Le Bourhis, T. Moxham, I. P. Dolbnya, A. M. Korsunsky, *Surface and Coatings Technology* **2020**, 381.

[8] C. Cao, H. F. Chan, J. Zang, K. W. Leong, X. Zhao, *Advanced materials* **2014**, 26, 1763.

[9] M. Amjadi, M. Sitti, *Adv Sci (Weinh)* **2018**, 5, 1800239.

[10] R. Tabassian, V. H. Nguyen, S. Umrao, M. Mahato, J. Kim, M. Porfiri, I. K. Oh, *Adv Sci (Weinh)* **2019**, 6, 1901711.

[11] L. Miao, J. Wan, Y. Song, H. Guo, H. Chen, X. Cheng, H. Zhang, *ACS Appl Mater Interfaces* **2019**, 11, 39219.

[12] R. Liu, X. Kuang, J. Deng, Y. C. Wang, A. C. Wang, W. Ding, Y. C. Lai, J. Chen, P. Wang, Z. Lin, H. J. Qi, B. Sun, Z. L. Wang, *Adv Mater* **2018**, 30.

[13] D. Chen, Q. Liu, Z. Han, J. Zhang, H. Song, K. Wang, Z. Song, S. Wen, Y. Zhou, C. Yan, Y. Shi, *Adv Sci (Weinh)* **2020**, 7, 2000584.

[14] S.-t. Xing, P.-p. Wang, S.-q. Liu, Y.-h. Xu, R.-m. Zheng, Z.-f. Deng, Z.-f. Peng, J.-y. Li, Y.-y. Wu, L. Liu, *Composites Science and Technology* **2020**, 193.

[15] P. Zhao, B. Xu, Y. Zhang, B. Li, H. Chen, *ACS Appl Mater Interfaces* **2020**, 12, 15716.

[16] P. Li, N. Su, Z. Wang, J. Qiu, *ACS Nano* **2021**, 15, 16811.

[17] Y. Zhao, C.-Y. Lo, L. Ruan, C.-H. Pi, C. Kim, Y. Alsaid, I. Frenkel, R. Rico, T.-C. Tsao, X. He, *Science Robotics* **2021**, 6, eabd5483.

[18] Y. F. Zhang, N. Zhang, H. Hingorani, N. Ding, D. Wang, C. Yuan, B. Zhang, G. Gu, Q. Ge, *Advanced Functional Materials* **2019**, 29.

[19] W. Shan, T. Lu, C. Majidi, *Smart Materials and Structures* **2013**, 22, 085005.

[20] D. Hwang, E. J. Barron III, A. T. Haque, M. D. Bartlett, *Science Robotics* **2022**, 7, eabg2171.

[21] J. A. Jackson, M. C. Messner, N. A. Dudukovic, W. L. Smith, L. Bekker, B. Moran, A. M. Golobic, A. J. Pascall, E. B. Duoss, K. J. Loh, *Science advances* **2018**, 4, eaau6419.

[22] C. Majidi, R. J. Wood, *Applied Physics Letters* **2010**, 97, 164104.

[23] A. Pettersson, S. Davis, J. O. Gray, T. J. Dodd, T. Ohlsson, *Journal of Food Engineering* **2010**, 98, 332.

[24] J. T. Auletta, G. J. LeDonne, K. C. Gronborg, C. D. Ladd, H. Liu, W. W. Clark, T. Y. Meyer, *Macromolecules* **2015**, 48, 1736.

[25] T. Li, J. Wang, L. Zhang, J. Yang, M. Yang, D. Zhu, X. Zhou, S. Handschuh-Wang, Y. Liu, X. Zhou, *Journal of Materials Chemistry B* **2017**, 5, 5726.

[26] S. Xiang, T. Li, W. Dong, Q. Lu, *Journal of Polymer Science Part B: Polymer Physics* **2018**, 56, 1469.
[27] T. Spratte, C. Arndt, I. Wacker, M. Hauck, R. Adelung, R. R. Schröder, F. Schütt, C. Selhuber-Unkel, *Advanced Intelligent Systems* **2022**, 4, 2100081.

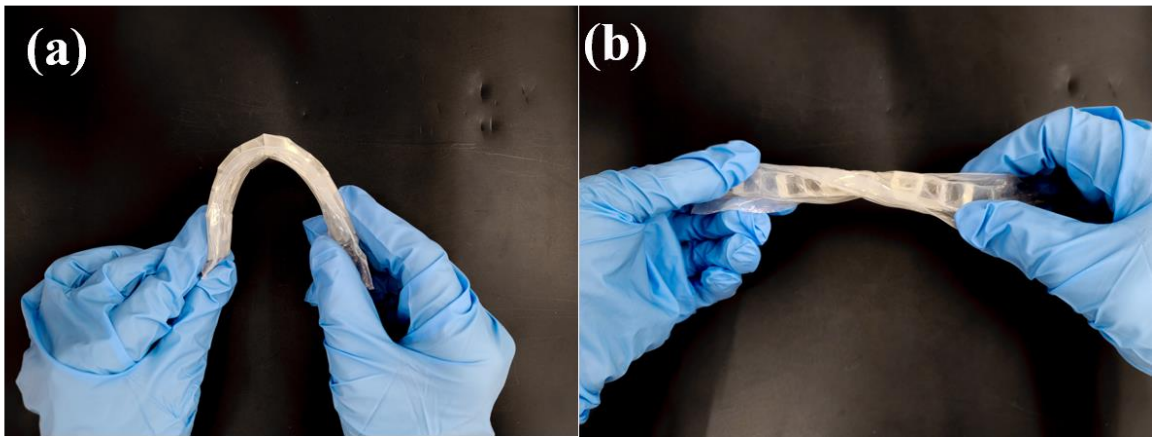


Figure S1 (a) Bending and (b) Twisting of our robotic materials

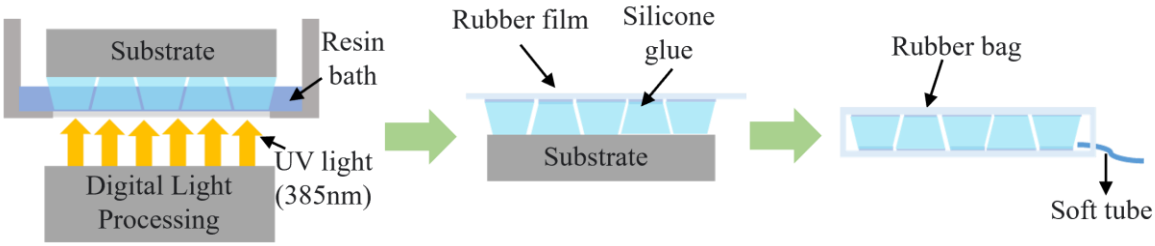


Figure S2 Fabrication process of robotic materials

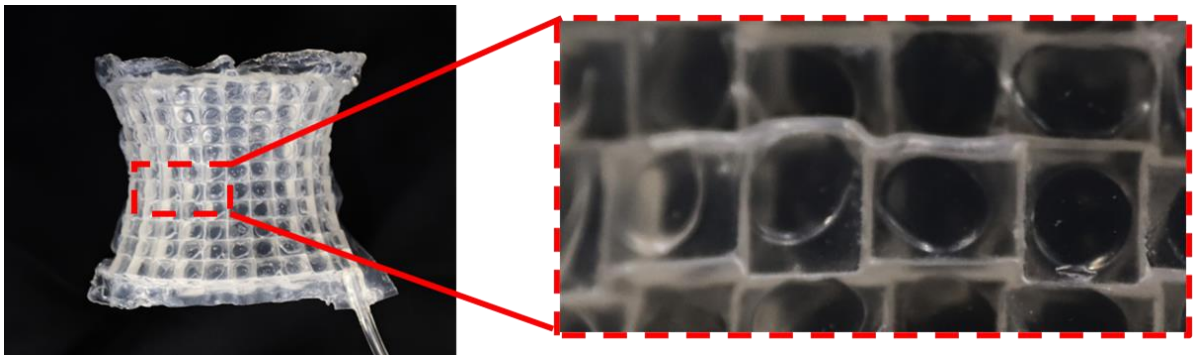


Figure S3. The deformation of rubber membranes under negative pressure in the saddle surface

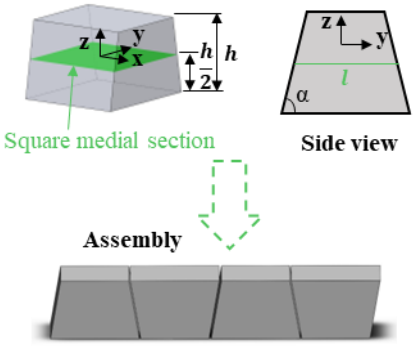


Figure S4 Geometrical design of architectured particles for three-point bending tests

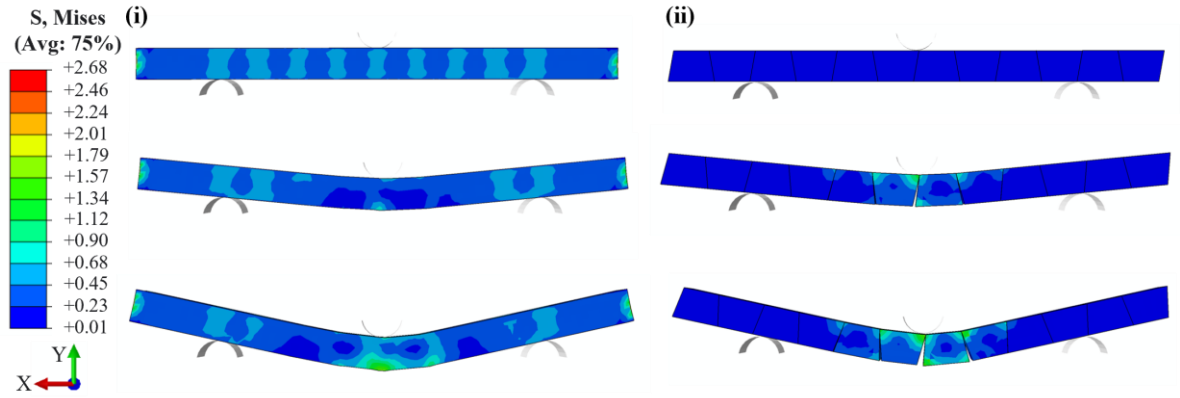


Figure S5 Finite element simulation images of our robotic materials under different loading displacements. (i) Images showing the deformation of the rubber bag; (ii) Images showing the deformation of internal particles.

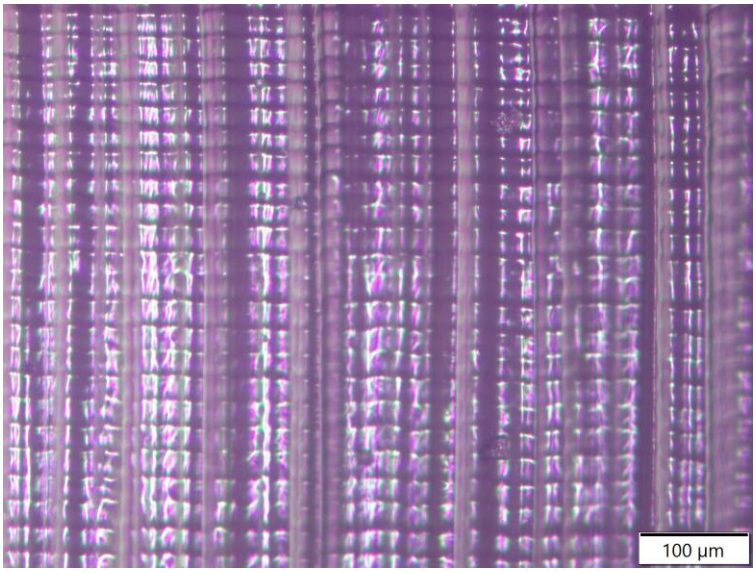


Figure S6 Optical images of the surface morphology of the conductive particle

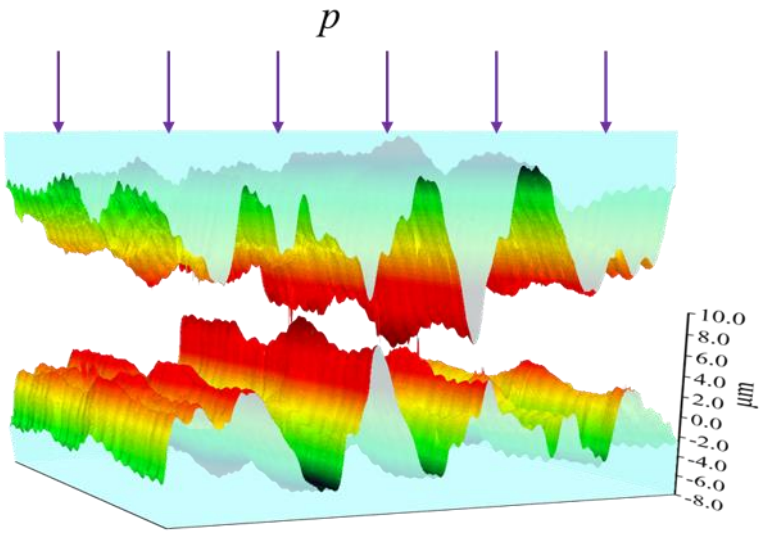


Figure S7 Plots showing the contact between two cubic particles, the data of the surface morphology is obtained from laser scanning confocal microscope

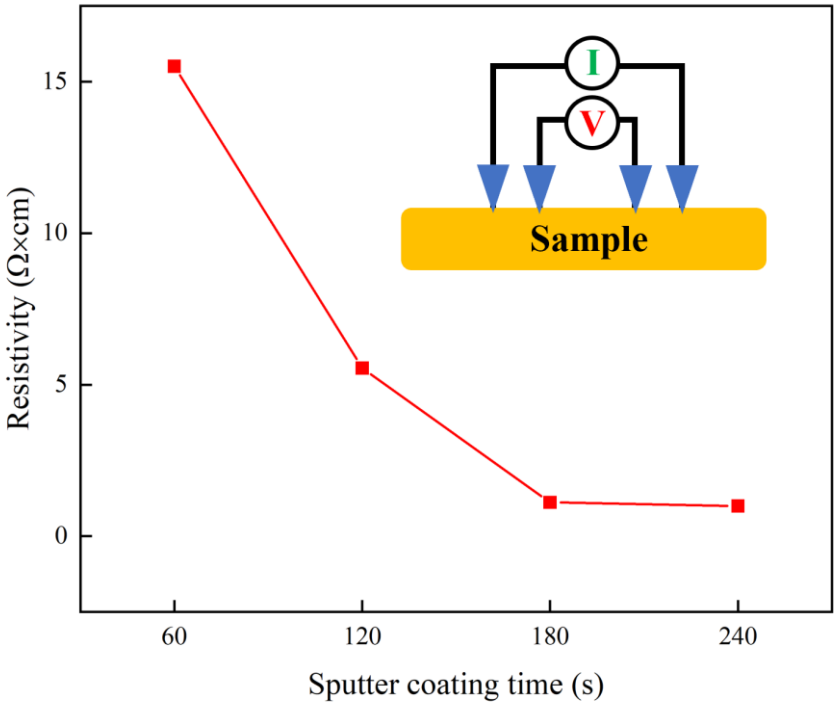


Figure S8 Resistivity of cubic sample as a function sputter coating time

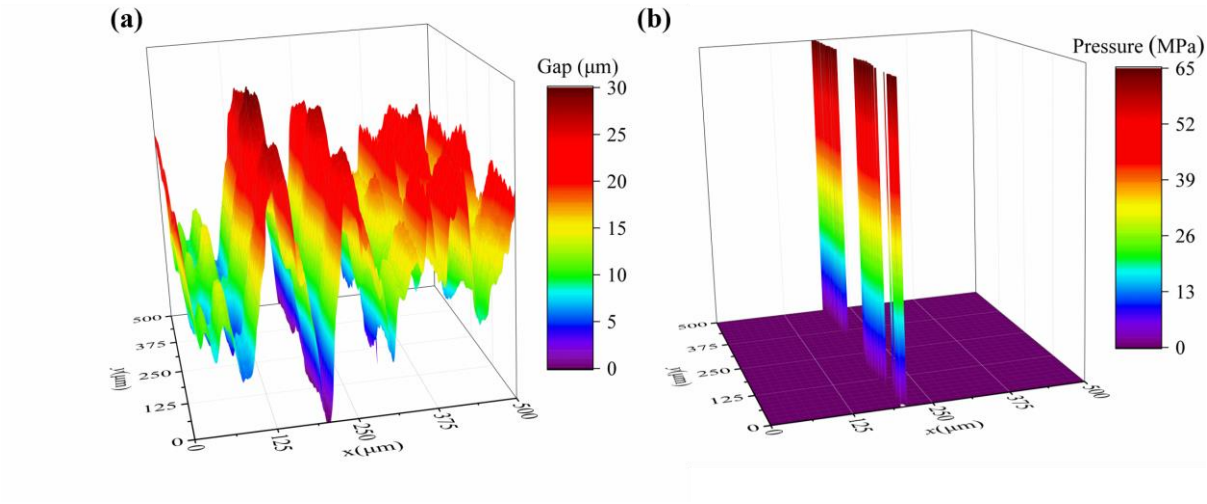


Figure S9 (a) Gap and (b) pressure distribution of cubic particle surface with coating

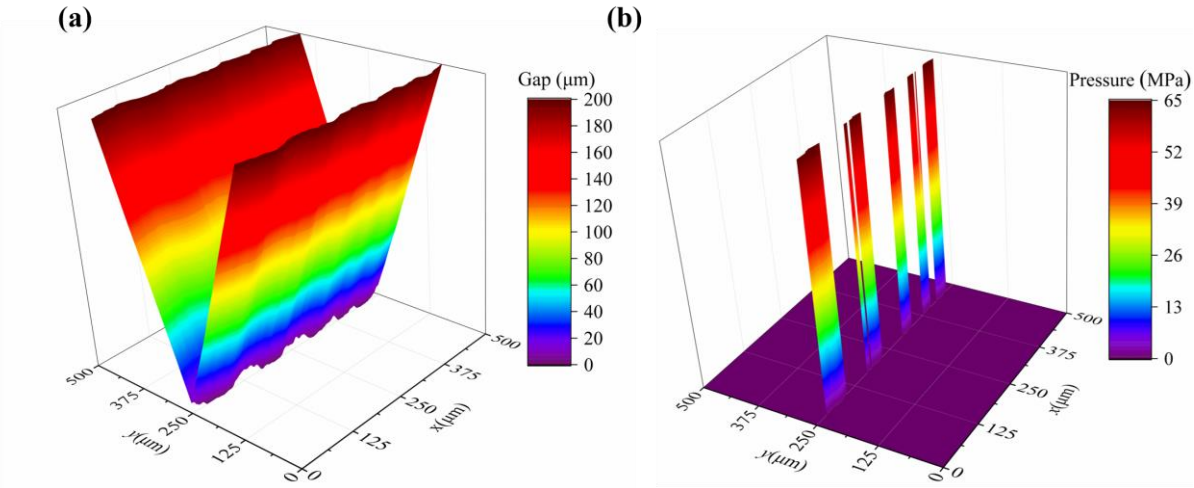


Figure S10 (a) Gap and (b) pressure distribution of trapezoidal particle surface with coating

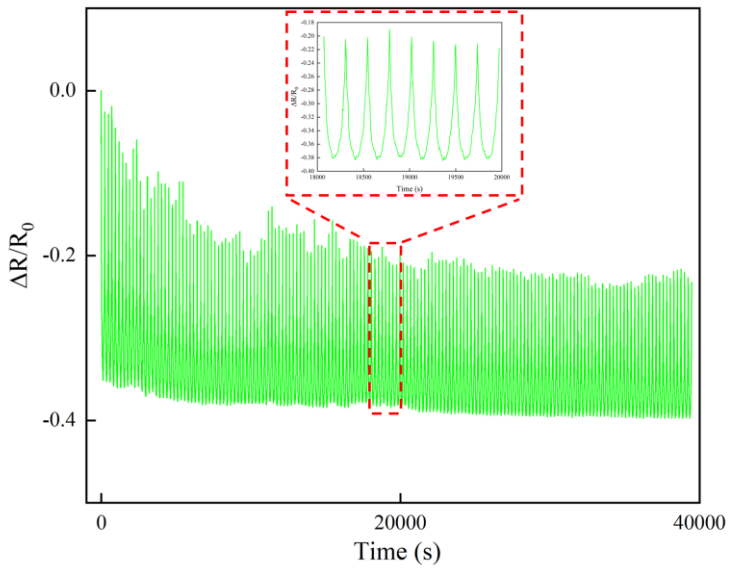


Figure S11 Stability test of the sensing performance

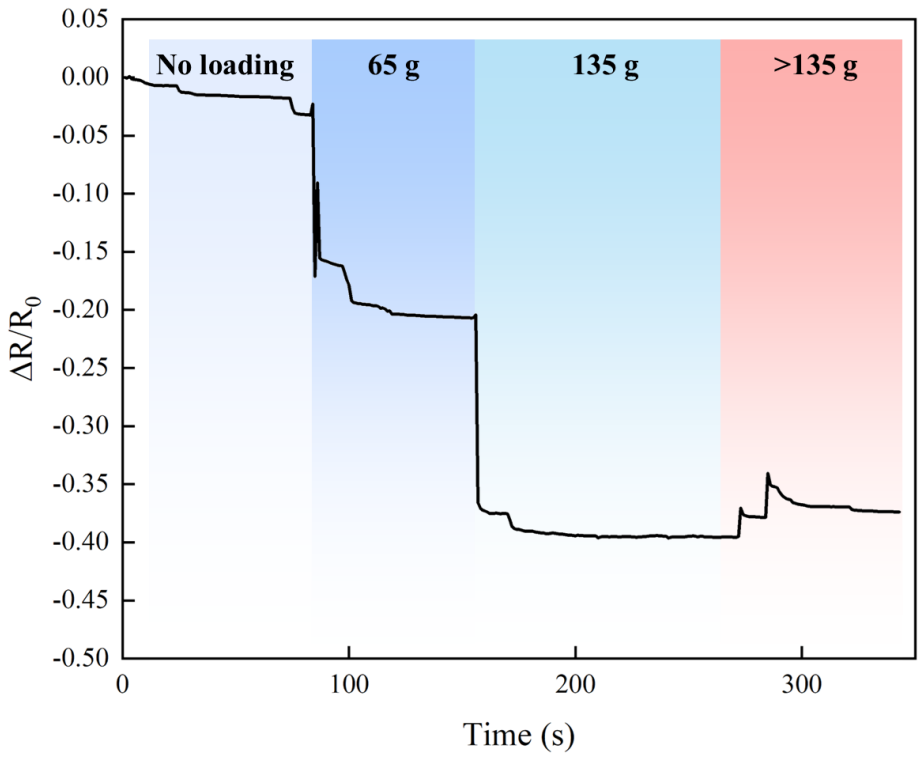


Figure S12 Weight sensing range of the gripper

Table S1 Comparison of recent works on self-sensing actuator

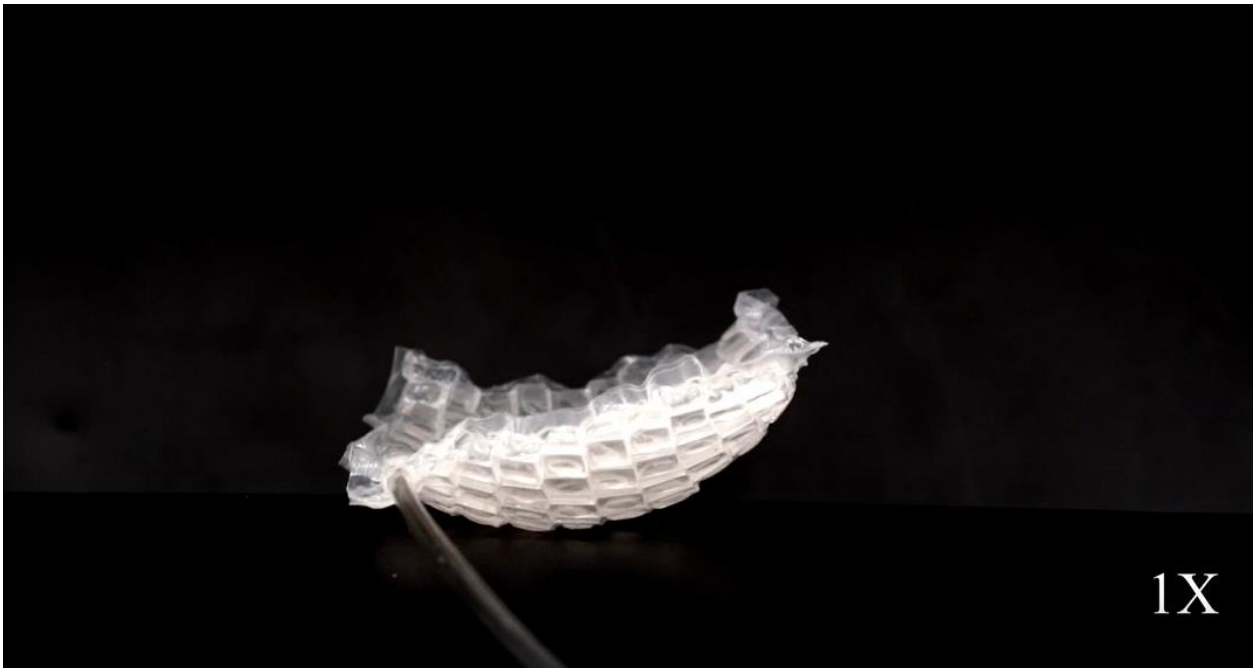
Materials	**Structure integration type**	**Actuation type**	**Sensing type**	**Actuation response time**	**Stiffness tuning (Yes/No)**	**Reference**
Graphite and carbon nanotubes, Paper, and Polypropylene plastic film	Two layers integration	Light and electrothermal	Piezoresistive	~25 s	No	[9]
Graphene, Cu foil and Nafion	Sandwich structure (Multiple layers)	Current	Piezorelectric	NA	No	[10]
Carbon nanofibers and polylactic acid	Sandwich structure (Multiple layers)	Electrothermal	Piezoresistive	78 ms	No	[11]
Polycaprolactone	Sandwich structure (Multiple layers)	Thermal	Piezorelectric	NA	Yes	[12]
Carbon black reinforced polylactic acid	Integrated within one material system	Thermal	Piezoresistive	NA	No	[13]
Shape memory polymer, sliver nanoparticles and polyvinyl alcohol	Sandwich structure (Multiple layers)	Thermal	Piezorelectric	40-50 s	Yes	[14]
Photonic crystal	Integrated within one material system	Electrothermal	Optical	~ 100 s	No	[15]
Polyethylene terephthalate, MXene and polystyrene sulfonic acid	Integrated within one material system	Moisture	Piezorelectric	NA	No	[16]
poly(N-isopropylacrylamide) and polyaniline	Integrated within one material system	Thermal	Piezoresistive	NA	No	[17]

Conductive architectured particles	Integrated within one material system	Pneumatic	Piezoresistive	~0.3 s	Yes	This work

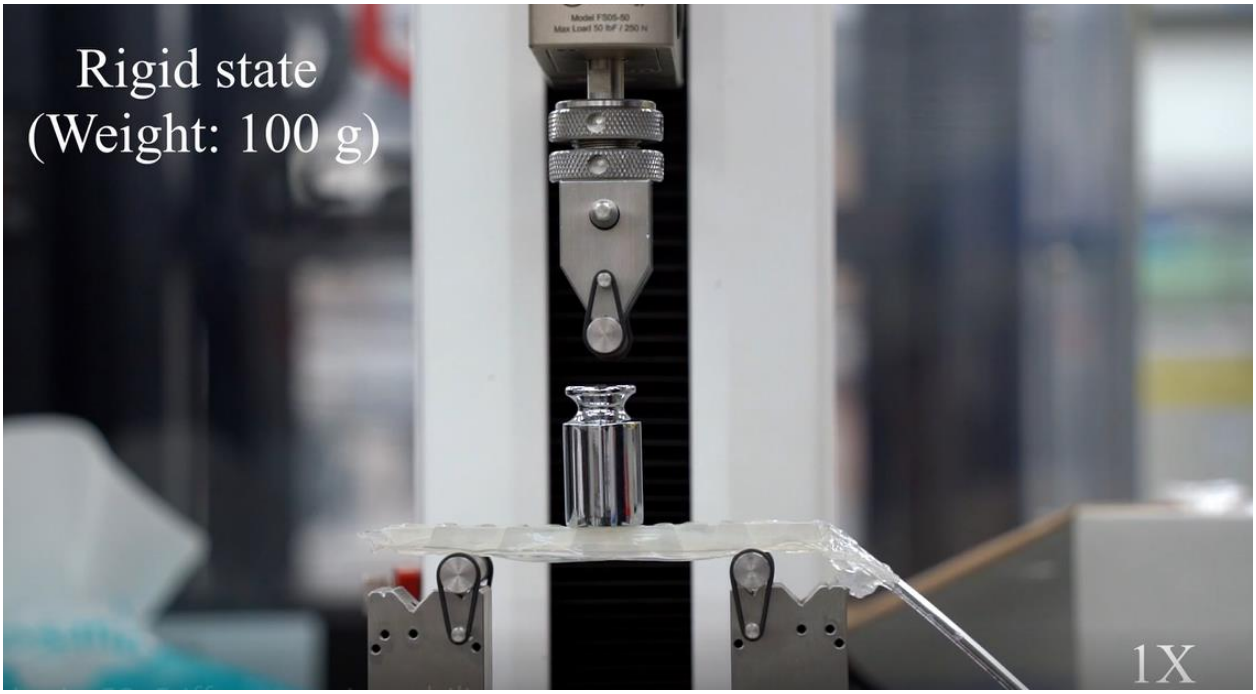
Table S2 Comparisons of variable-stiffness materials actuated by different methods

Classification	Materials	Dimensions	Response time	Apparent modulus range	Ref.
Thermal actuated materials	Shape memory polymers	108mm x 22.5 mm x 20.9 mm	~32 s	10 MPa~1 GPa	[18]
	Thermal composites	50 mm x 15 mm x 4.5 mm	~68 s	108 kPa~0.9 GPa	[19]
	Liquid metals	~100 mm x 100 mm x1.76 mm	~90 s	30 MPa~3 GPa	[20]
Magnetic actuated materials	Magnetorheological fluid	10 mm x10 mm x 10 mm	~0.83 s	0.15 MPa~0.2 MPa	[21]
	Magnetorheological fluid	60 mm x 10 mm x 5 mm	~0.17 s	0.1644 MPa~1.4658 MPa	[22]
	Magnetorheological fluid	NA	~0.15 s	3 kPa~60kPa	[23]
Chemical actuated materials	Hydrogels	25 mm x 25 mm x 3.8 mm	~135 min	1 Mpa~3.8 Mpa	[24]
	Hydrogels	25 mm x 15 mm x 2 mm	~ 60 min	0.58 Mpa~2.9 Mpa	[25]
	Hydrogels	15 mm x 4 mm x 2mm	NA	0.086 MPa~45.6 MPa	[26]
	Hydrogels	Cylinder shaped, Diameter: 8 mm; Height: 12 mm	~ 60 s	4 kPa~81 kPa	[27]

Movie S1. Shape morphing ability of robotic structures



Movie S2. Stiffness tunability of robotic structures



Movie S3. Self-sensing ability of robotic structures

